Progress in Physics of Applied Materials 7 (2027), Serial Number 14, 95-109

Semnan University

Progress in Physics of Applied Materials

journal homepage: https://ppam.semnan.ac.ir/

Effect of Annealing Time on Spin-Coated ZnO Thin Film Properties

Monneka Fiacre Kouide [a,b], Mazabalo Baneto [a,b,*], Ognanmi Ako [a,b], Alphonse Déssoudji Gboglo [a,b], Abdoul-Razak Ali-Tagba [a,b], Shafi Ullah [c], Bernabé Marí [c]

[a] *Centre d'Excellence Régional pour la Maîtrise de l'Electricité (CERME), Université de Lomé, 01BP 1515, Lomé, Togo*
[b] *Laboratoire sur l'Energie Solaire, Département de physique, Faculté des Sciences, Université de Lomé, 01BP 1515, Lomé, Togo*
[c] *Department de Física Aplicada-IDF, Universitat Politècnica de València, Camí de Vera s/n, 46022 València, Spain*

ARTICLE INFO

Article history:
Received: 8 May 2026
Revised: 1 July 2026
Accepted: 10 July 2026
Published online: 2 September 2026

Keyword:
Thin film;
Zinc oxide;
Annealing time;
Spin coating;
Physical properties.

ABSTRACT

This study investigates the effect of annealing time on the physical properties of spin-coated zinc oxide (ZnO) thin films. Zinc acetate dihydrate, ethanol, and monoethanolamine were used as the precursor, solvent, and stabilizer, respectively. The films were deposited on glass substrates at 2500 rpm for 30 s, followed by pre-annealing at 200 °C for 5 min and final annealing at 400 °C for durations ranging from 1 to 5 h at 1 h intervals. X-ray diffraction analysis confirmed that all deposited films were polycrystalline and exhibited a hexagonal wurtzite crystal structure. The preferential orientation along the (002) plane and the crystallite size increased with annealing time up to 3 h, followed by a slight decrease at longer annealing durations. Field-emission scanning electron microscopy revealed that annealing time significantly affected the surface morphology of the films. The film annealed for 1 h exhibited a relatively smooth and homogeneous surface with a few microcracks, suggesting incomplete grain growth. In contrast, films annealed for 2–5 h showed increased surface heterogeneity associated with the formation of relief-like surface features. Photoluminescence analysis revealed visible emission dominated by a green luminescence band. The films annealed for 3 and 5 h exhibited a lower defect density, whereas those annealed for 1, 2, and 4 h showed a higher density of defect-related states. Energy-dispersive X-ray spectroscopy confirmed the elemental composition of the ZnO films. UV–Vis spectroscopy revealed that all samples exhibited optical transmittance in the visible region, with optical band gap values ranging from 3.23 to 3.36 eV. Overall, an annealing time of 3 h provided the best balance among the structural, morphological, and optical properties of the ZnO thin film.

1. Introduction

Transparent conductive oxides (TCOs) have gained considerable importance in solar cells in recent years, owing to their high transmission of visible light and good electrical conductivity [1]. In perovskite solar cells in particular, the choice of TCO is critical, as it directly influences charge collection as well as the overall device efficiency [2–4]. To date, several materials have been investigated. Tin dioxide (SnO_2) has been studied extensively due to its wide bandgap and high electron mobility [5]. Nevertheless, SnO_2 undergoes surface hydroxylation under ambient conditions, leading to the formation of unsaturated tin dangling bonds that act as non-radiative recombination centers and contribute to hysteresis losses [6]. Tungsten trioxide (WO_3) exhibits good optical transparency and a high specific surface area; however, its application is limited by a reduction in open-circuit voltage and increased charge recombination losses [4]. Indium oxide (In_2O_3) is another promising n-type semiconductor featuring a wide band gap (3.75 eV), an electron mobility of 20 $cm^2 \cdot V^{-1} \cdot s^{-1}$, as well as excellent thermal stability and good transparency in the visible range [4]; nevertheless, it suffers from poor

* Corresponding author.
E-mail address: mazbaneto@gmail.com

Cite this article as:
Kouide, F.M., Baneto, M., Ako, O., Gboglo, A.D., Ali-Tagba, A.R., Ullahc, S., and Marí, B., 2027. Effect of Annealing Time on Spin-Coated ZnO Thin Film Properties. *Progress in Physics of Applied Materials*, *7*(1), pp.95-109.DOI: 10.22075/ppam.2026.41142.1224

surface coverage of the deposited film, which compromises the uniformity and compactness required for efficient charge extraction [7]. Cerium oxide (CeO_x) is a rare-earth oxide characterized by a wide band gap (3.5 eV), high ionic conductivity, a large dielectric constant, and good thermal and chemical stability [7]; however, it's very low electron mobility (~0.01 $cm^2 \cdot V^{-1} \cdot s^{-1}$) severely limits efficient charge transport toward the collecting electrode [7,8]. Titanium dioxide (TiO_2) is a semiconductor featuring high optical transparency in the visible range, excellent chemical stability, and favorable energy level alignment with perovskite absorbers [9,10]. It is the most widely used material as an electron transport layer in perovskite solar cells. However, its relatively low electron mobility (0.1–4 $cm^2 \cdot V^{-1} \cdot s^{-1}$) [11] and susceptibility to ultraviolet-induced degradation limit charge transport and compromise the long-term stability of photovoltaic devices [12]. In this context, zinc oxide (ZnO) emerges as a promising alternative to TiO_2, primarily due to its high electron mobility, which can reach up to 205 $cm^2 \cdot V^{-1} \cdot s^{-1}$ [13]. This property promotes fast and efficient charge transport. Furthermore, ZnO possesses excellent optical transparency [14], which further supports its appeal as an electron transport layer in perovskite solar cells. In addition, this II–VI group semiconductor exhibits a wide variety of nanostructures [15], enabling improved contact with perovskite thin films. However, it has been reported [16–19] that the physical properties of ZnO thin films depend heavily on the synthesis conditions. Several methods for synthesizing ZnO have been used in the literature, including hydrothermal [20–24], spray pyrolysis [25–27], chemical bath deposition [28–32], thermal evaporation under vacuum [33–36], and sol-gel [37–41]. The sol-gel method, with its two deposition techniques, dip coating [42] and spin coating [43–45], stands out from other methods due to its simplicity and low cost. The structural, morphological, and optical properties of ZnO thin films obtained by this method are influenced by several parameters, including the nature of the precursor [46–48], the stabilizer [49–51], the solvent [52], the concentration of the solution [53,54], annealing temperature [55–59], and annealing time [60,61]. The effect of annealing time on the physical properties of ZnO thin films has been extensively investigated in the literature . Mathew et al. [62] showed that the preferred orientation along the (002) plane strengthens with increasing annealing time, accompanied by a decrease in the optical band gap. Similarly, Kumar et al. [61] observed an improvement in the (002) orientation, together with increases in crystallite size and surface roughness. In contrast, Motlan et al. [63] reported a different dominant orientation, mainly along the (101) plane. Furthermore, Toe et al. [60] highlighted an opposite trend in the optical properties, namely a gradual increase in the band gap with increasing annealing time. Although these studies confirm the importance of annealing time in tuning the structural, morphological, and optical properties of ZnO, the optimal conditions required to achieve a balance among these properties remain unclear, particularly for thin films prepared by the sol–gel spin-coating method.

In this context, the present study provides a complementary contribution by simultaneously analyzing the evolution of the structural, morphological, and optical properties of ZnO as a function of annealing duration in order to better understand the correlations between crystallographic orientation, grain growth, and optical behavior under controlled synthesis conditions.

2. Material and methods

2.1. Materials and Reagents

Microscope glass slides were used as substrates for the deposition of ZnO thin films. Zinc acetate dihydrate ($Zn(CH_3COO)2 \cdot 2H_2O$, 99.99%, Sigma-Aldrich) was used as the precursor, while absolute ethanol (CH_3CH_2OH, 99.98%, VWR International) served as the solvent. Monoethanolamine (MEA, C_2H_7NO, 99.99%, Sigma-Aldrich) was used as a stabilizing agent to control the hydrolysis and condensation reactions during sol preparation. All chemicals were used as received without further purification.

2.2. Cleaning of Substrates

The glass substrates (2.5 cm × 2.0 cm) were cleaned in an ultrasonic bath for 15 min per step. Initially, the substrates were immersed in a detergent solution to remove surface contaminants adsorbed from ambient air. They were then sequentially rinsed with acetone, ethanol, and distilled water to eliminate organic and inorganic residues, and finally dried in an oven.

2.3. ZnO Thin Films Synthesis

ZnO thin films were deposited on glass substrates using the spin-coating technique. A 0.4 mol/L sol–gel solution was prepared by dissolving an appropriate amount of zinc acetate in absolute ethanol, followed by the addition of monoethanolamine (MEA) as a stabilizing agent, with a MEA/Zn precursor molar ratio of 1. After magnetic stirring at 60 °C for 1 h, the resulting homogeneous and transparent solution was aged for 24 h. The films were deposited at 2500 rpm for 30 s, followed by a pre-annealing step at 200 °C for 5 min to evaporate the solvent and remove residual organic species. This deposition/pre-annealing cycle was repeated four times. The final annealing temperature was fixed at 400 °C based on the work of Guo et al. [64]. The films were subsequently annealed at 400 °C for 1, 2, 3, 4, and 5 h to investigate the effect of annealing duration on the structural, morphological, and optical properties of ZnO thin films. The obtained samples were labeled according to annealing duration as 1 h, 2 h, 3 h, 4 h, and 5 h, respectively.

2.4. Characterization of ZnO Thin Films

The fabricated ZnO thin films were characterized using several analytical techniques to investigate their structural, morphological, compositional, and optical properties. X-ray diffraction (XRD, Rigaku Ultima IV, λ = 1.5406 Å, Cu Kα radiation) was used to determine the crystalline structure and phase composition. Diffraction

patterns were recorded in the 2θ range from 10° to 80°. Field-emission scanning electron microscopy (FE-SEM) was performed using a Zeiss ULTRA 55 microscope equipped with an in-lens secondary electron (SE) detector to examine the surface morphology of the films. The instrument was coupled with an energy-dispersive X-ray (EDX) spectroscopy system for elemental composition analysis. EDX measurements were carried out at an accelerating voltage of 15 kV. The optical properties of the ZnO thin films were investigated using UV–Vis spectroscopy (Ocean Optics DT-MINI-2-GS spectrometer) in the wavelength range from 300 to 800 nm. Photoluminescence (PL) spectra were recorded using an Ocean Optics spectrometer equipped with a 405 nm diode laser as the excitation source.

3. Results and Discussion

3.1. Structural Characterization

X-ray diffraction was employed to determine the crystalline structure of the spin-coated ZnO thin films. Figure 1 shows the XRD patterns of films annealed at 400 °C for 1–5 h. Eight well-defined diffraction peaks were observed at 2θ = 31.82°, 34.44°, 36.28°, 47.64°, 56.67°, 62.96°, 67.92°, and 72.36°, corresponding to the (100), (002), (101), (102), (110), (103), (112), and (004) crystallographic planes, respectively. These peaks are consistent with the hexagonal wurtzite structure of ZnO (space group $P6_3mc$), in agreement with JCPDS card 36-1451 [65]. Furthermore, these results indicate that the films are polycrystalline. No additional peaks corresponding to secondary phases were detected, confirming that the films consist solely of ZnO. The results also show that annealing time has a significant effect on the XRD patterns of the ZnO thin films. In particular, an increase in the preferential growth along the (002) plane is observed with increasing annealing time, reaching a maximum at 3 h, followed by a sharp decrease and subsequent stabilization at longer annealing durations. ZnO generally grows along the (002) direction due to the low surface free energy of this plane, which provides a thermodynamic driving force and leads to improved crystallinity [58,66,67]. Thermal annealing supplies the energy required for atoms to overcome the activation barrier for diffusion and occupy energetically favorable lattice sites, thereby promoting the growth of grains with lower surface energy. With increasing annealing time, small grains progressively merge to form larger grains. Grains oriented along the (002) plane, benefiting from this energetic advantage, grow faster than others, leading to an enhancement of this orientation up to 3 h of annealing [61,62].

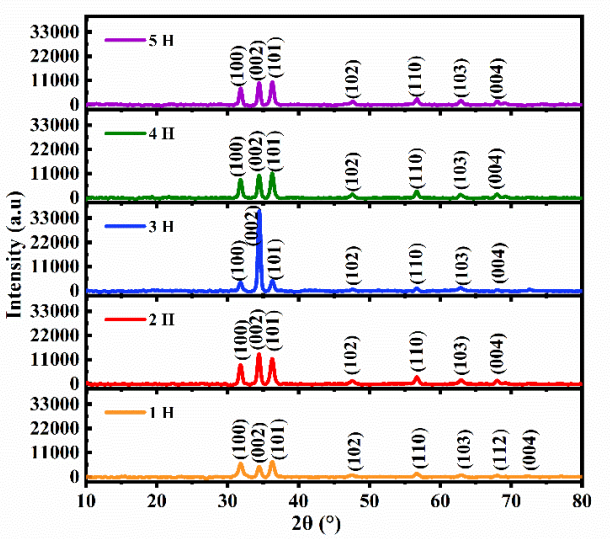

Fig. 1. XRD patterns of ZnO thin films obtained at different annealing times

The strong decrease in the intensity of the (002) peak beyond 3 h may be attributed to a partial degradation of the preferred orientation or to structural reorganization of the thin films [58].

To confirm this preferential growth, the texture coefficient $T_{C(hkl)}$ was calculated for the three most dominant peaks using Equation (1) [68,69]:

$$T_{c\,(hkl)} = \frac{\frac{I_{(hkl)}}{I_{o_{(hkl)}}}}{\frac{1}{n}\sum \frac{I_{(hkl)}}{I_{o_{(hkl)}}}} \quad (1)$$

where $I_{(hkl)}$, n, and $I_{0(hkl)}$ represent the X-ray diffraction peak intensities obtained from the thin films, the number of diffraction peaks considered (in this case n=3), and the reference diffraction peak intensities (JCPDS 36-1451 [65]), corresponding to randomly oriented grains, respectively. The results are presented in Table 1.

Table 1. Texture coefficient of ZnO thin films obtained at different annealing times along the dominant planes (100), (002), and (101).

Annealing time	$T_{c\,(hkl)}$		
	(100)	(002)	(101)
1 H	1.140	1.121	0.738
2 H	0.796	1.605	0.599
3 H	0.222	2.629	0.149
4 H	0.894	1.426	0.680
5 H	0.851	1.467	0.681

The calculation of the texture coefficient (T_c) for the (100), (002), and (101) planes, based on the corresponding diffraction peaks presented in Table 1, shows that the T_C value is greater than 1 for the (002) plane, regardless of the annealing time. However, for films annealed for 1 h, a particular situation is observed.

It is clearly seen from Table 1 that $T_{C(100)}$ is slightly higher than $T_{C(002)}$, with a very small difference (≈ 0.019). This negligible difference indicates a weak texture, where crystallographic orientations are still competing, although a (002) preferred orientation begins to emerge. With increasing annealing time, $T_{C(002)}$ becomes progressively dominant and reaches a maximum value at 3 h, indicating a strong c-axis-oriented crystallization. However, for annealing durations longer than 3 h, the (002) texture slightly decreases. These results are consistent with those obtained from the XRD patterns.

The lattice parameters a and c of the thin films annealed at 400 °C for different annealing times were calculated using Equation (2), and the interplanar spacing (d) was determined using Bragg's law given in Equation (3) [70]:

$$a = \sqrt{\frac{1}{3}}\frac{\lambda}{sin\theta} \text{ and } c = \frac{\lambda}{sin\theta} \quad (2)$$

$$d = \frac{\lambda}{2sin\theta} \quad (3)$$

where λ is the wavelength of the CuKα radiation (1.54059 Å) and θ is the diffraction peak angle. The obtained results are presented in Table 2. The values of the lattice parameters a and c, as well as the interplanar spacing d, are consistent with the reference values reported in JCPDS card 36-1451. The value of the ratio c/a ≈ 1.602, obtained for all the samples, confirms the hexagonal wurtzite structure [65].

Table 2. Lattice parameters and structural properties of ZnO thin films obtained at different annealing times.

Rotation time	2θ (°)	I (a.u)	β (°)	D–S method		W-H method		ε ×10³	Lattice parameters			d (Å)	V (Å³)	L (Å)
				D (nm)	δ ×10¹⁵ Lines /m²	D (nm)	δ ×10¹⁵ Lines /m²		a (Å)	c (Å)	c/a			
1 H	34.46	4582.96	0.659	12.627	6.272	11.375	7.730	-0.661	3.245	5.201	1.603	2.601	47.420	1.975
2 H	34.42	13526.34	0.576	14.435	4.799	17.967	3.098	1.260	3.245	5.207	1.605	2.603	47.474	1.976
3 H	34.46	36166.52	0.468	17.760	3.170	20.541	2.371	1.380	3.247	5.201	1.602	2.601	47.479	1.976
4 H	34.44	10235.66	0.490	16.957	3.478	17.158	3.397	0.400	3.245	5.204	1.604	2.602	47.448	1.975
5 H	34.44	9818.62	0.484	17.201	3.380	20.254	2.438	1.540	3.243	5.204	1.605	2.602	47.448	1.975
JCPDS card 36-1451	34.42	-	-	-	-	-	-	-	3.250	5.207	1.602	2.603	47.622	-

In addition, the effect of annealing time on the (002) peak intensity, crystallite size, dislocation density, full width at half maximum (FWHM), average crystallite size, lattice strain, unit cell volume, and bond length was investigated. The (002) peak intensity values are presented in Table 1. As shown in this table, a progressive and significant increase is observed, reaching a maximum at 3 h, corresponding to an intensity approximately 7.9 times higher than that measured at 1 h. This evolution indicates a marked improvement in the crystallinity of the films. Beyond 3 h, a pronounced decrease in this intensity is observed.

The crystallite size (D) of the thin films, determined along the dominant (002) peak, was calculated using the Debye–Scherrer (D–S) formula, as given in Equation (4). [71]:

$$D = \frac{k\lambda}{\beta cos\theta} \quad (4)$$

where k is a constant equal to 0.9, λ is the wavelength of the X-ray source (1.54059 Å), β is the FWHM of the diffraction peak, and θ is the Bragg diffraction angle. The crystallite size values for different annealing durations are reported in Table 2. A general increase in crystallite size is observed from 1 to 5 h of annealing, rising from 12.627 nm to 17.201 nm. These results are in good agreement with those reported by Motlan et al. [63], who also observed an increase with annealing time. This behavior is attributed to thermal energy, which enhances atomic diffusion and grain coalescence, promoting crystallite growth. The effect is more pronounced between 1 and 3 h, indicating improved crystallization [72]. Beyond 3 h, only slight variations are observed, suggesting a quasi-equilibrium state where grain growth tends to stabilize.

The dislocation density (δ), which reflects the defect concentration within the crystal lattice, was estimated using Equation (5) [70], where the crystallite size (D) was determined from the Debye–Scherrer method.

$$\delta = \frac{1}{D^2} \quad (5)$$

Fig. 2 shows the evolution of the dislocation density of ZnO thin films obtained at different annealing times. As shown in Figure 2, the dislocation density decreases significantly as the annealing time increases from 1 to 3h and then exhibits slight fluctuations for longer annealing durations. This behavior indicates that the film annealed for 3 h possesses the lowest density of structural defects. Figure 3 shows the evolution of the FWHM obtained at different annealing times. As shown in Figure 3, the full

width at half maximum (β) of the (002) peak decreases significantly as the annealing time increases from 1 to 3 h, indicating a marked improvement in crystallinity. The films annealed for 3 h therefore exhibit the highest crystalline quality, consistent with the strong preferred orientation along the (002) plane. Beyond 3 h, a slight increase in β is observed at 4 h, followed by a decrease at 5 h.

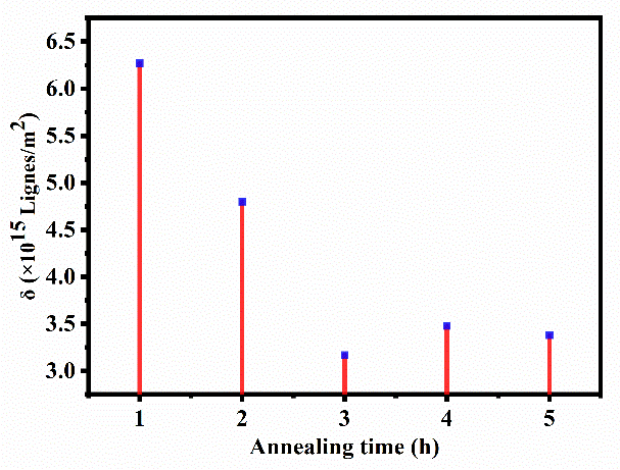

Fig. 2. Dislocation density variation of ZnO thin films obtained at different annealing times.

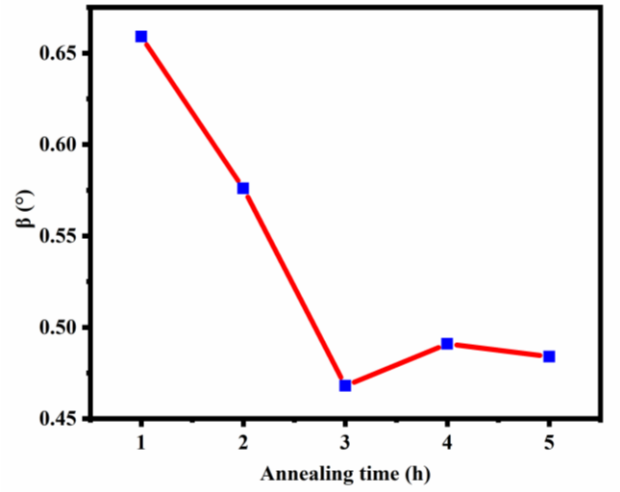

Fig. 3. FWHM variation of ZnO thin films obtained at different annealing times.

These results are consistent with the variations in crystallite size and dislocation density discussed above.

To further analyze the effects of size and strain on peak broadening, Williamson–Hall (W–H) analysis was employed. The W–H method separates the size-induced and strain induced broadening contributions based on the following equation(6) [73,74]:

$$\beta cos\theta = \frac{k\lambda}{D} + 4\varepsilon sin\theta \quad (6)$$

where β is the FWHM, θ is the peak position, λ =1.54059 Å, k is a constant equal to 0.9, D is the crystallite size, and ε is the lattice microstrain. In this method, $\beta \cos\theta$ is plotted against 4sinθ; the slope of the linear fit provides the strain ε, while the intercept is used to determine D.

Fig. 4 shows the Williamson–Hall plot (βcos vs. 4sinθ) used to evaluate both crystallite size and lattice microstrain in ZnO films. The microstrain exhibits a clear dependence on annealing time. As shown in Figure 4, the film annealed for 1 h, a negative value is obtained, indicating compressive stress associated with residual strain prior to thermal relaxation [75]. With increasing annealing time (2–5 h), the microstrain becomes positive, suggesting a transition toward tensile behavior driven by crystal growth and atomic rearrangement [75]. This change correlates well with the evolution of preferred orientation, reflecting a balance between stress relaxation and microstructural reorganization during annealing.

The crystallite size extracted from the Williamson–Hall analysis also shows a pronounced evolution with annealing time. It increases from 11.375 nm (1 h) to 17.967 nm (2 h), reaching a maximum of 20.541 nm at 3 h, indicating enhanced crystallinity and grain growth [76]. This behavior is attributed to crystallite coalescence and defect reduction during the early stages of annealing. Beyond 3 h, a decrease is observed at 4 h (17.158 nm), followed by a recovery at 5 h (20.254 nm), suggesting a competition between grain growth and structural relaxation under prolonged annealing. Both the Debye–Scherrer and Williamson–Hall methods exhibit a similar overall trend, with crystallite size increasing up to 3 h of annealing, followed by stabilization or minor fluctuations, indicating improved crystallinity of the ZnO films. However, the Williamson–Hall method yields higher values since it accounts for both crystallite size and lattice strain, unlike the Debye–Scherrer method, which considers only size broadening. Despite this difference, both approaches consistently identify the 3 h-annealed sample as having the best crystalline quality.

The values of the defect density calculated using the Williamson–Hall method and presented in Table 2 show a decrease as the annealing time increases from 1 to 3 h, followed by a slight increase at 4 h before decreasing again at 5 h. The Williamson–Hall results follow the same overall trend as those of the Scherrer method. These findings are consistent with the XRD analysis (FWHM, peak intensity, and texture coefficient), confirming that the film annealed for 3 h exhibits the best crystalline quality, with maximum crystallite size, reduced microstrain, and strong (002) preferred orientation.

The unit cell volume (V) of the hexagonal wurtzite structure was calculated using Equation (7) [77,78].

$$\beta cos\theta = \frac{k\lambda}{D} + 4\varepsilon sin\theta \quad (7)$$

Fig. 5 shows the variation of the unit cell volume of ZnO thin films obtained at different annealing times. As shown in this figure, the unit cell volume increases with annealing time from 1 to 3 h, reaching a maximum at 3 h. Beyond this point, a decrease is observed up to 4 h, followed by a slight stabilization at 5 h. Since the highest value is obtained at 3 h, this annealing time also corresponds to the most pronounced (002) preferred

orientation and the maximum crystallite size, suggesting a more ordered crystal growth at this stage [79].

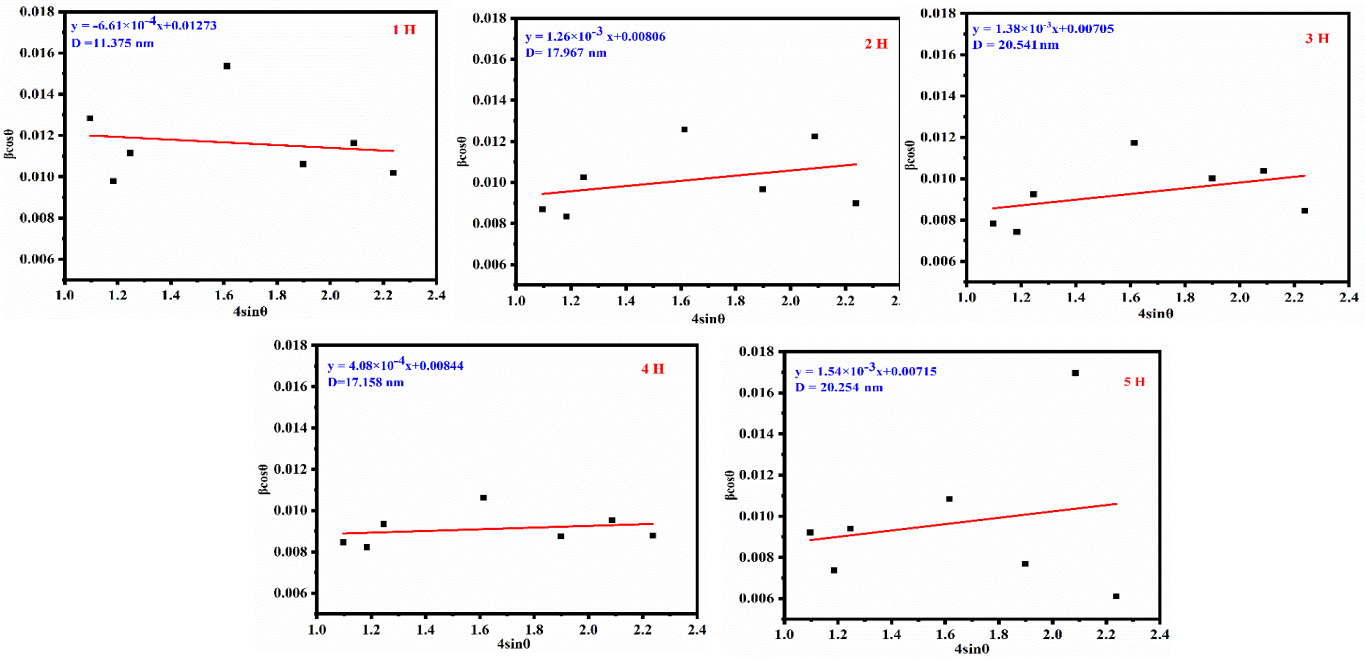

Fig. 4. Williamson–Hall plot (βcosθ vs. 4sinθ) of ZnO thin films obtained at different annealing times.

The Zn-O bond length (L) was estimated using Equation (10) [77,78], where u, the internal parameter, represents the positional parameter of the wurtzite structure. This parameter describes the relative displacement of atoms with respect to the adjacent plane along the c-axis and is given by Equation (8).

$$L = \sqrt{\frac{a^2}{3} + \left(\frac{1}{2} - u\right)^2 c^2} \quad (8)$$

$$u = \frac{a^2}{3c^2} + 0.25 \quad (9)$$

The results show that the Zn–O bond length (L) is approximately 1.975 Å and remains nearly constant despite increasing annealing time. This indicates that the local atomic arrangement is essentially stable, highlighting the robustness of the Zn–O bond in the wurtzite structure. Overall, these results suggest that the structural properties of the obtained thin films are influenced by annealing time.

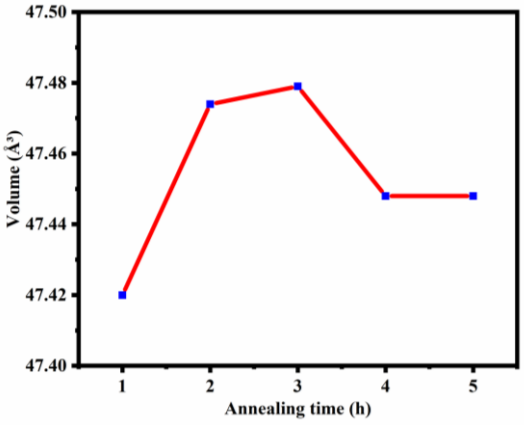

Fig. 5. Unit cell volume of ZnO thin films obtained at different annealing times.

3.2. Morphological Properties

Fig. 6 shows the FESEM images of ZnO thin films annealed at 400 °C for different durations. A progressive evolution of the surface morphology is observed with increasing annealing time. For an annealing time of 1 h (Fig. 6a), the film surface appears relatively compact, consisting of very fine, poorly developed grains, with a few microcracks and weakly defined surface features, indicating limited atomic diffusion [56,57,80]. When the annealing time increases to 2 h (Fig. 6b), the surface exhibits increased roughness and heterogeneity, characterized by the formation of aggregates and morphological irregularities. The appearance of these features suggests the onset of thermally activated diffusion, promoting grain growth and progressive

coalescence [81]. At 3 h of annealing (Fig. 6c), the ZnO film surface shows a granular structure composed of relatively uniform, densely packed nanograins. These morphological features result in higher surface roughness due to enhanced grain coalescence under thermal treatment, indicating more advanced crystallization and densification of the films [82]. This morphology suggests that prolonged annealing promotes structural reorganization, leading to a more textured surface and improved grain development [61]. For 4 h of annealing (Fig. 6d), the surface features are well developed and uniformly distributed across the film, indicating significant nanograin coalescence and a strongly textured morphology. In contrast, at 5 h of annealing (Fig. 6e), although the surface features remain visible, the morphology becomes slightly less homogeneous, which may be attributed to excessive grain growth or the development of internal stresses induced by prolonged annealing. These results are in good agreement with those reported by Toe et al. [60], who observed that short annealing durations lead to fine and compact particles. In contrast, larger particles develop as the annealing time increases. This behavior is generally attributed to the Ostwald ripening phenomenon, in which smaller, thermodynamically less stable particles gradually dissolve and redeposit onto larger ones, resulting in grain growth.

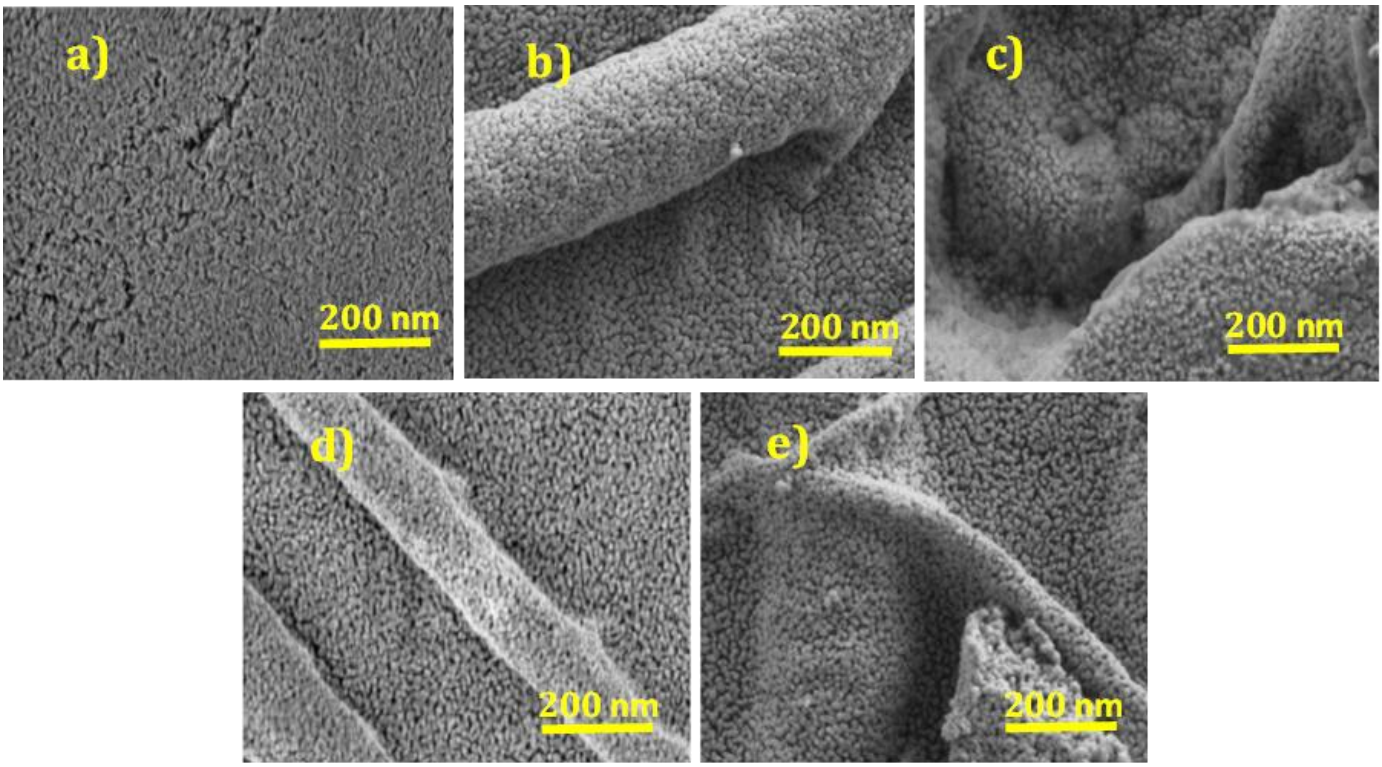

Fig. 6. FE-SEM images of ZnO thin films obtained at different annealing times: a) 1 h, b) 2 h**,** c) 3 h, d) 4 h, and e) 5 h**.**

3.3. Chemical Composition by EDX Analysis Using Scanning Electron Microscope

Fig. 7 presents the EDS spectra of ZnO thin films annealed at 400 °C for different annealing durations.

The spectra clearly confirm the chemical composition of zinc oxide through the presence of characteristic zinc and oxygen peaks, indicating that the films are properly formed [83]. The silicon signal is attributed to the glass substrate [84,85]. In contrast to the work of Kumar et al. [61], who observed substrate diffusion at longer annealing times, the presence of Si only in the sample annealed for 1 h can be explained by diffusion from the glass substrate through grain boundaries and structural defects, particularly the microcracks observed by FE-SEM. Grain boundaries and extended defects are widely recognized as preferential pathways for atomic diffusion in ZnO thin films [86]. Similarly, Ghica et al. [87] demonstrated that annealing-induced diffusion along grain boundaries in ZnO films can promote the segregation and localization of impurity species in defect-rich regions. Thus, at the initial stage of annealing, the high defect density and the presence of microcracks facilitate Si migration into the ZnO thin. For longer annealing durations (2–5 h), densification and improved crystallinity reduce diffusion pathways, thereby limiting silicon incorporation.

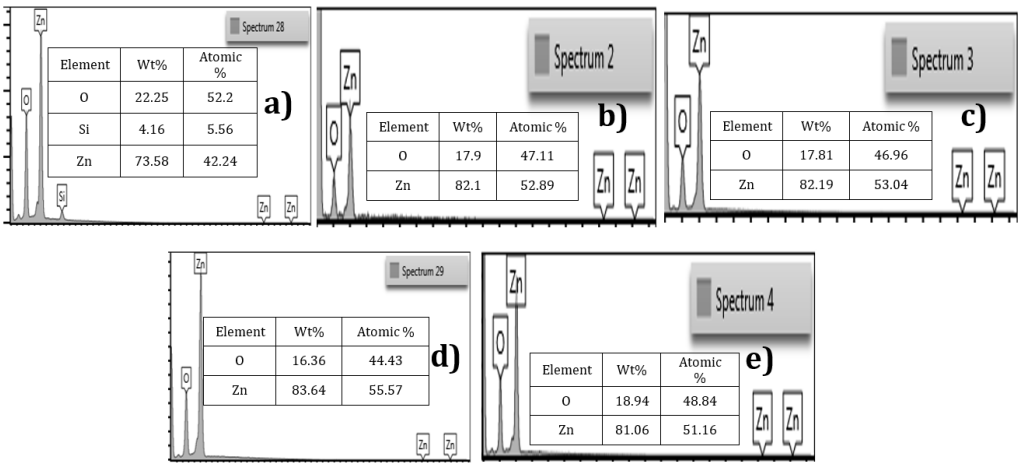

Fig. 7. EDX spectra of ZnO thin films obtained at different annealing times.

3.4. Photoluminescence

Fig. 8 shows the photoluminescence (PL) spectra of ZnO thin films annealed at 400 °C for different annealing times, in the wavelength range of 300–900 nm. The films exhibit visible emissions (400–780 nm) regardless of the annealing duration. In the literature, these emissions are commonly attributed to intrinsic or extrinsic defects in ZnO [88]. Oxygen vacancies (V_O), zinc vacancies (V_{Zn}), interstitial oxygen (O_i), interstitial zinc (Zn_i), oxygen antisites (O_{Zn}), and zinc antisites (Zn_O) constitute intrinsic defects, also referred to as native defects constitute intrinsic defects, also referred to as native defects [89]. To enable a more precise identification of emission centers, the obtained PL spectra were deconvoluted using Gaussian fitting to analyze impurity-related defects. Figure 9 shows the deconvoluted PL spectra of ZnO thin films annealed at 400 °C for different annealing times.

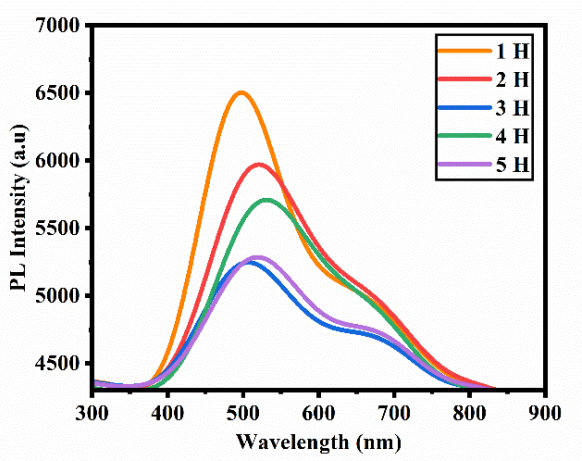

Fig. 8. Photoluminescence spectra of ZnO thin films obtained at different annealing times.

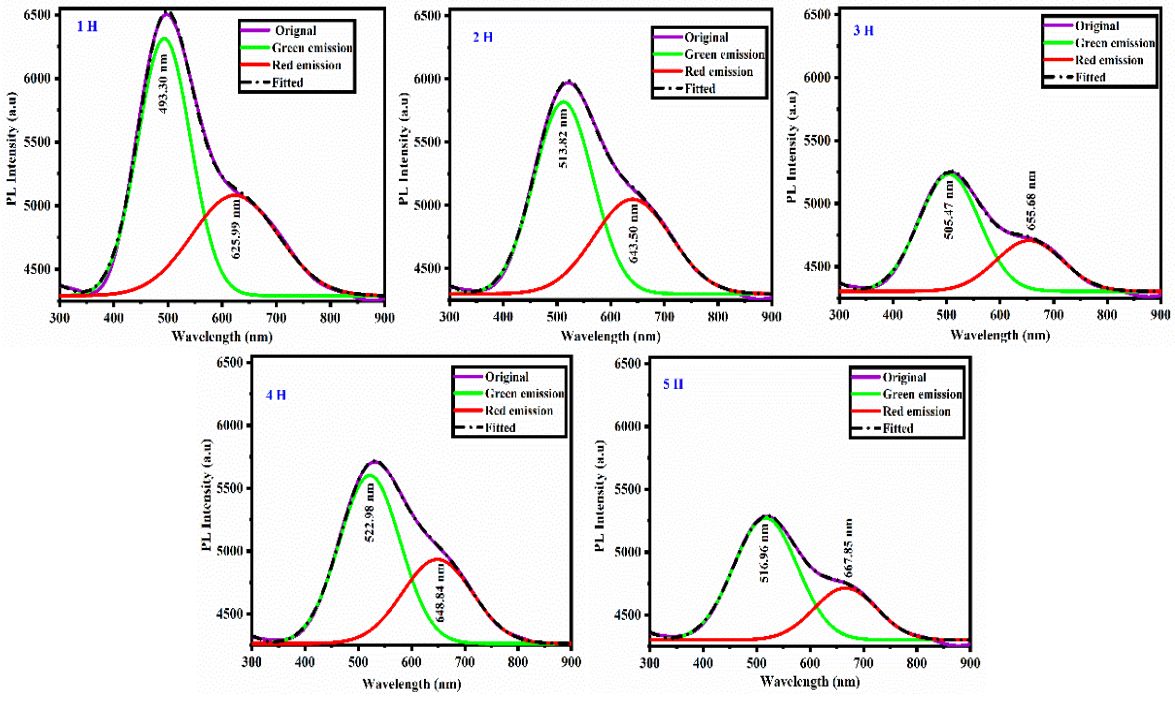

Fig. 9. Deconvoluted photoluminescence spectra of ZnO thin films obtained at different annealing times.

Fig. 9 clearly shows two main visible emissions, with peak positions varying as a function of annealing time. The first emission exhibits peaks centered at 493.30 nm, 513.82 nm, 505.47 nm, 522.98 nm, and 516.96 nm for annealing times of 1 h, 2 h, 3 h, 4 h, and 5 h, respectively. These photoluminescence peaks correspond to the characteristic green emission of ZnO [90,91]. This emission is commonly attributed to radiative transitions involving intrinsic lattice defects such as oxygen vacancies (V_O), zinc interstitials (Zn_i), and other surface-related defects [92,93]. The second emission is located in the red region of the spectrum, with peak positions at 625.99 nm, 643.50 nm, 655.68 nm, 648.84 nm, and 667.85 nm for samples annealed for 1 h, 2 h, 3 h, 4 h, and 5 h, respectively. This band is attributed to oxygen interstitials (O_i) as well as oxygen vacancies (V_O) [94]. The evolution of both emission bands indicates that samples annealed for 1 h exhibit the highest defect-related intensities, reflecting a high density of recombination centers. This observation is consistent with the XRD and FE-SEM analyses, which reveal a high dislocation density and the presence of microcracks, indicating a highly disturbed crystal lattice. Samples annealed for 2 h and 4 h also show relatively strong defect-related emissions, suggesting a significant, although reduced, defect concentration compared to that of the 1 h sample. the 1 h sample. In contrast, samples annealed for 3 h and 5 h exhibit lower photoluminescence intensities, indicating a reduced defect density within the crystal structure

Therefore, the thin films annealed for 3 h and 5 h, which exhibit lower defect densities, appear more suitable for photovoltaic applications.

3.5. UV-Visible

To investigate the optical properties of ZnO thin films, UV–Visible transmittance measurements were performed in the wavelength range of 300–800 nm, as shown in Figure 10. The curves show a sharp increase in transmittance between 350 and 400 nm, corresponding to the optical absorption edge of ZnO associated with its wide band gap (~3.3 eV). Beyond this region, the films become highly transparent in the visible range. In this region, transmittance exceeds 50%, confirming the good optical transparency of ZnO. The sample annealed for 1 h exhibits the highest value, reaching nearly 95%, indicating low optical absorption and high film quality. Such transparency is particularly important for ZnO used as an electron transport layer (ETL) in solar cells, as it ensures efficient light transmission to the active layer, enhancing electron–hole pair generation and photovoltaic performance. This behavior agrees well with the FE-SEM observations, which reveal smooth and uniform surfaces for this sample.

In contrast, the samples annealed for 2 h, 4 h, and 5 h display similar optical behavior, with transmittance values ranging from approximately 35% to 80%. A gradual increase is observed between 400 and 600 nm, followed by stabilization at higher wavelengths. The reduced transmittance in these samples is attributed to increased surface roughness and the presence of aggregates, as observed by FE-SEM, which enhance light scattering and consequently reduce optical transmission [95]. The sample annealed for 3 h exhibits a transmittance of about 80%, slightly higher than that of the 2 h, 4 h, and 5 h samples, but still lower than that of the film annealed for 1 h. This behavior can be attributed to its improved crystallinity and relatively favorable surface morphology.

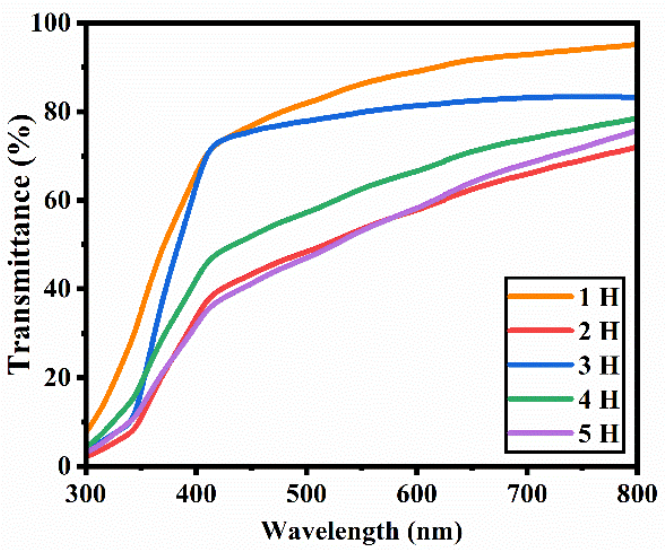

Fig. 10. Transmittance spectra of ZnO thin films obtained at different annealing times.

3.6. Band Gap Energies

The optical band gap energy (Eg) was estimated from the absorption spectra using Tauc's Equation [78,96]:

$$(\alpha h\upsilon)^n = A\left(h\upsilon - E_g\right) \quad (10)$$

where α, hν, Eg, and A represent the absorption coefficient, photon energy, optical band gap energy, and a constant, respectively. A direct allowed transition was assumed for ZnO (n = 2), in agreement with its direct band gap nature.

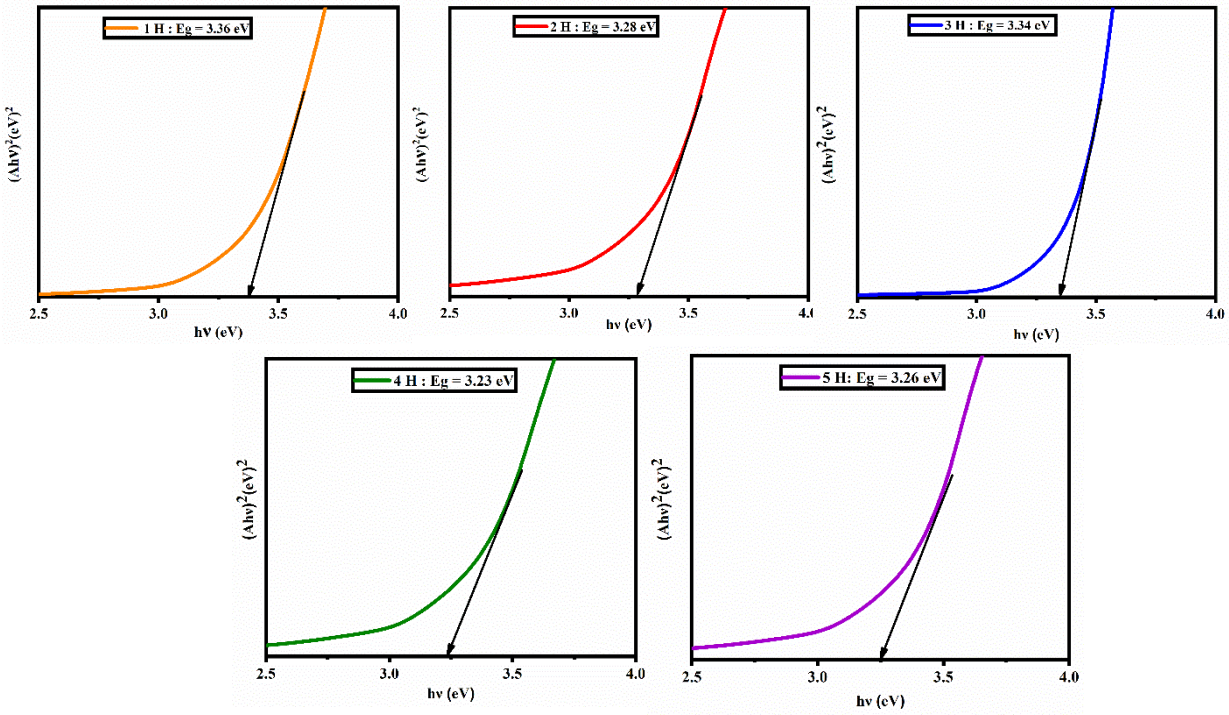

Fig. 11. Band gap energy of thin films obtained at different annealing times.

In this study, the optical analysis was performed using the measured absorbance as an approximation of the absorption coefficient. According to the Beer–Lambert law, the absorbance is directly proportional to the absorption coefficient for a given film thickness [97]. Therefore, although the absolute value of the absorption coefficient could not be determined due to the absence of thickness measurements, the absorbance preserves the spectral dependence of the optical absorption. Consequently, the optical band gap was estimated using Tauc plots constructed by plotting $(Ahν)^2$ as a function of the photon energy (hν) .

The linear region was selected near the fundamental absorption edge and extrapolated to determine Eg. Figure 11 shows the band gap energy of ZnO thin films obtained at different annealing times. The band gap values for films annealed from 1 to 5 h are 3.36, 3.28, 3.34, 3.23, and 3.26 eV, respectively. The band gap ranges from 3.23 to 3.36 eV over all samples. These values are lower than that of bulk ZnO (3.37 eV). This difference is attributed to the crystallite size, crystalline quality, surface morphology, residual stress, and structural defects of the different thin films [56,62,63,72,98,99]. Thus, thin films annealed for 3 hours combine high optical transparency reaching 80 % in the visible range and a bandgap energy of approximately 3.34 eV, which would make them suitable for use as electron transport layers in solar cells.

4. Conclusion

Zinc oxide thin films were spin-coated onto glass substrates to investigate the effect of annealing time (1–5 h) on their structural, morphological, and optical properties. XRD analysis confirmed that all films are polycrystalline with a hexagonal wurtzite structure, with the film annealed for 3 h exhibiting improved crystallinity and a preferred (002) orientation. The crystallite size increased with annealing time. FESEM observations revealed that prolonged annealing promotes grain growth and coalescence, leading to changes in surface morphology; the film annealed for 1 h exhibited a smooth surface with minor microcracks, whereas films annealed for 2–5 h showed increased surface heterogeneity. Photoluminescence analysis indicated a lower defect density in the films annealed for 3 h and 5 h. EDX confirmed the ZnO composition, while UV–Vis spectroscopy showed that optical transmittance decreased with annealing time (from approximately 95% at 1 h to about 80% at 3 h), with band gap values ranging from 3.23 to 3.36 eV, slightly lower than that of bulk ZnO (3.37 eV) due to structural defects and internal stresses. Overall, an annealing time of 3 h was identified as optimal for achieving ZnO thin films with a balanced combination of structural, morphological, and optical properties.

Acknowledgements

The authors gratefully acknowledge the Centre d'Excellence Régional pour la Maîtrise de l'Électricité (CERME), University of Lomé, for financial and institutional support, and the Erasmus+ KA107 programme for mobility funding. This work was also supported by the project "Advanced Macro- and Micro-Additive Manufacturing Technologies: Towards a New Hydrogen Application in Sustainable Mobility" (CIPROM/2022/3, Competitive Research Projects, Generalitat Valenciana).

Funding Statement

This research received no external funding.

Conflicts of Interest

The authors declare that they have no known competing financial interests or personal relationships that could have appeared to influence the work reported in this paper.

Author Contribution Statement

Conceptualization, M.F.K., M.B. and O.A.; Methodology, M.F.K. and M.B.; Formal analysis, A.D.G., A.A., S.U. and B.M.; Data curation, M.F.K., O.A., S.U. and B.M.; Writing—original draft, M.F.K.; Writing—review and editing, M.B., A.D.G., S.U. and B.M.; Visualization, A.D.G. and A.A; Supervision, M.B. All authors have read and agreed to the published version of the manuscript.

References

[1] Ikhmayies, S.J., 2017. Transparent Conducting Oxides for Solar Cell Applications. *Mediterranean Green Buildings & Renewable Energy* ed A. Sayigh (Cham: Springer International Publishing), pp. 899–907.

[2] Wei, Q., Yang, Z., Yang, D., Zi, W., Ren, X., Liu, Y., Liu, X., Feng, J. and (Frank) Liu, S., 2016. The effect of transparent conductive oxide on the performance CH3NH3PbI3 perovskite solar cell without electron/hole selective layers. *Solar Energy*, 135, pp.654–661.

[3] Dou, B., Miller, E.M., Christians, J.A., Sanehira, E.M., Klein, T.R., Barnes, F.S., Shaheen, S.E., Garner, S.M., Ghosh, S., Mallick, A., Basak, D. and Van Hest, M.F.A.M., 2017. High-Performance Flexible Perovskite Solar Cells on Ultrathin Glass: Implications of the TCO. *Journal of Physical Chemistry Letters*, 8, pp.4960–4966.

[4] Zainal Abidin, N.A., Arith, F., Noorasid, N.S., Sarkawi, H., Mustafa, A.N., Safie, N.E., Shah, A.S.M., Azam, M.A., Chelvanathan, P. and Amin, N., 2023. Dopant engineering for ZnO electron transport layer towards efficient perovskite solar cells. *RSC Advances*, 13, pp.33797–33819.

[5] Ye, J., Li, Y., Medjahed, A.A., Pouget, S., Aldakov, D., Liu, Y. and Reiss, P., 2023. Enhanced performance of planar perovskite solar cells by doping the SnO2 electron transport layer with guanidinium chloride. *Frontiers in Materials*, 10, p.1118641.

[6] Ning, X., Wang, Y., Ren, X., Guo, H., Yang, H., Wei, J., Guo, J., Li, T., Zhu, C. and Hou, F., 2024. ZnO/SnO2 bilayer electron transport layer strategy to improve the performance of FAPbI3 solar cell. *Journal of Applied Physics*, 135, p.015301.

[7] Sharma, H. and Srivastava, R., 2023. Solution-processed pristine metal oxides as electron-transporting materials for perovskite solar cells. *Frontiers in Electronic Materials*, 3, p.1174159.

[8] Suzuki, T., Kosacki, I., Anderson, H.U. and Colomban, P., 2001. Electrical Conductivity and Lattice Defects in Nanocrystalline Cerium Oxide Thin Films. *Journal of the American Ceramic Society*, 84, pp.2007–2014.

[9] Mali, S.S., Hong, C.K., Inamdar, A.I., Im, H. and Shim, S.E., 2017. Efficient planar n-i-p type heterojunction flexible perovskite solar cells with sputtered TiO_2 electron transporting layers. *Nanoscale*, 9, pp.3095–3104.

[10] Shahiduzzaman, Md., Kuwahara, D., Nakano, M., Karakawa, M., Takahashi, K., Nunzi, J-M. and Taima, T., 2020. Low-Temperature Processed TiOx Electron Transport Layer for Efficient Planar Perovskite Solar Cells. *Nanomaterials*, 10, p.1676.

[11] Zhang, P., Wu, J., Zhang, T., Wang, Y., Liu, D., Chen, H., Ji, L., Liu, C., Ahmad, W., Chen, Z.D. and Li, S., 2018. Perovskite Solar Cells with ZnO Electron-Transporting. *Materials Advanced Materials*, 30, p.1703737.

[12] Ji, J., Liu, X., Jiang, H., Duan, M., Liu, B., Huang, H., Wei, D., Li, Y. and Li, M., 2020. Two-Stage Ultraviolet Degradation of Perovskite Solar Cells Induced by the Oxygen Vacancy-Ti4+ States. *iScience*, 23, p.101013.

[13] Look, D.C., Reynolds, D.C., Sizelove, J.R., Jones, R.L., Litton, C.W., Cantwell, G. and Harsch, W.C., 1998. Electrical properties of bulk ZnO Solid. *State Communications*, 105, pp.399–401.

[14] Navin, K. and Kurchania, R., 2015. Structural, morphological and optical studies of ripple-structured ZnO thin films. *Applied Physics A*, 121, pp.1155–1161.

[15] Manabeng, M., Mwankemwa, B.S., Ocaya, R.O., Motaung, T.E. and Malevu, T.D., 2022. A Review of the Impact of Zinc Oxide Nanostructure Morphology on Perovskite Solar Cell Performance. *Processes*, 10, p.1803.

[16] Sánchez-Dena, O., Hernández-López, S., Camacho-López, M.A., Acuña-Ávila, P.E., Reyes-Esqueda, J.A. and Vigueras-Santiago, E., 2022. ZnO Films from Thermal Oxidation of Zn Films: Effect of the Thickness of the Precursor Films on the Structural, Morphological, and Optical Properties of the Products. *Crystals*, 12, p.528.

[17] Yergaliuly, G., Soltabayev, B., Kalybekkyzy, S., Bakenov, Z. and Mentbayeva, A., 2022. Effect of thickness and reaction media on properties of ZnO thin films by SILAR. *Scientific Reports*, 12, p.851.

[18] Abdallah, B., Zetoun, W. and Tello, A., 2024. Deposition of ZnO thin films with different powers using RF magnetron sputtering method: Structural, electrical and optical study. *Heliyon*, 10, p.27606.

[19] Toma, F.T.Z., Rahman, M.S. and Maria, K.H., 2025. A review of recent advances in ZnO nanostructured thin films by various deposition techniques. *Discover Materials*, 5.

[20] Rosowska, J., Kaszewski, J., Krajewski, M., Małolepszy, A., Witkowski, B.S., Wachnicki, Ł., Bulyk, L-I., Sybilski, P., Godlewski, M. and Godlewski, M.M., 2025. Growth of ZnO Nanoparticles Using Microwave Hydrothermal Method—Search for Defect-Free Particles. *Nanomaterials*, 15, p.230.

[21] Anaya-Zavaleta, J.C., Ledezma-Pérez, A.S., Gallardo-Vega, C., Rodríguez-Hernández, J., Alvarado-Canché, C.N., García-Casillas, P.E., De León, A. and Herrera-May, A.L., 2025. ZnO Nanoparticles by Hydrothermal Method: Synthesis and Characterization. *Technologies*, 13, p.18.

[22] Abdel-Fattah, E.M., Alshehri, S.M., Alotibi, S., Alyami, M. and Abdelhameed, D., 2024. Hydrothermal Synthesis of ZnO Nanoflowers: Exploring the

Relationship between Morphology, Defects, and Photocatalytic Activity. *Crystals*, 14, p.892.

[23] Almamari, M.R., Ahmed, N.M., Holi, A.M., Yam, F.K., Kyaw, H.H., Almessiere, M.A. and Al-Abri, M.Z., 2022. Some Distinct Attributes of ZnO Nanorods Arrays: Effects of Varying Hydrothermal Growth Time. *Materials*, 15, p.5827.

[24] Kimiagar, S. and Mirazimi, H., 2024. Hydrothermal synthesis of Fe3 O4-ZnO nanocomposites for removing fluoride from water. *Progress in Physics of Applied Materials*, 4, pp.83–91.

[25] Bancheva-Koleva, P., Zhelev, V., Petkov, P. and Petkova, T., 2025. Indium-Doped ZnO Thin Films Obtained Using Spray Pyrolysis for Position-Sensitive Photodetection. *Materials*, 18, p.3744.

[26] Rabeel, M., Javed, S., Khan, R., Akram, M.A., Rehman, S., Kim, D. and Khan, M.F., 2022. Controlling the Wettability of ZnO Thin Films by Spray Pyrolysis for Photocatalytic Applications. *Materials*, 15, p.3364.

[27] Valdés, M., Villegas, E.A., Ramajo, L.A. and Parra, R., 2024. Ultraviolet-Sensor Based on Tin-Doped Zinc Oxide Thin Films Grown by Spray Pyrolysis. *Ceramics*, 7, pp.1500–1152.

[28] Cepero-Rodríguez, J.B., Ramos-Brito, F., Angulo-Rocha, J.N., Sánchez-Alejó, M.A., Martínez-Martínez, R., Camarillo-García, E., Lizárraga-Medina, E., Sánchez-Rodríguez, F.J., Alejo-Armenta, C., Canizalez-Román, A., Castillo, S.J., Molina-Duarte, J.J. and García-Hipólito, M., 2025. Electric Field-Assisted Chemical Bath Deposition of ZnO Thin Films: Effects of Field Intensity, Polarity Inversion, and Air Agitation on Film Properties. *Coatings*, 15, p.1225.

[29] Ruvalcaba-Manzo, S.G., Ramírez-Bon, R., Ochoa-Landín, R. and Castillo, S.J., 2025. A Comprehensive Study of the Optical, Structural, and Morphological Properties of Chemically Deposited ZnO Thin Films. *Inorganics*, 13, p.331.

[30] Baillard, A., Appert, E., Wilhelm, F., Sarigiannidou, E. and Consonni, V., 2025. Towards the Removal of HMTA Molecules in the Chemical Bath Deposition of ZnO Nanowires. *Nanomaterials*, 15, p.1574.

[31] Abitaev, K., Atanasova, P., Bill, J., Preisig, N., Kuzmenko, I., Ilavsky, J., Liu, Y. and Sottmann, T., 2023. In Situ Ultra-Small- and Small-Angle X-ray Scattering Study of ZnO Nanoparticle Formation and Growth through Chemical Bath Deposition in the Presence of Polyvinylpyrrolidone. *Nanomaterials*, 13, p.2180.

[32] Wai, H.S., Ikuta, T. and Li, C., 2024. Synthesis of AZO-Coated ZnO Core–Shell Nanorods by Mist Chemical Vapor Deposition for Wastewater Treatment Applications. *Molecules*, 29, p.309.

[33] Fouad, O., Ismail, A., Zaki, Z. and Mohamed, R., 2006. Zinc oxide thin films prepared by thermal evaporation deposition and its photocatalytic activity. *Applied Catalysis B: Environmental*, 62, pp.144–149.

[34] Thach, P.H. and Khai, T.V., 2023. Thermal Evaporation Synthesis, Optical and Gas-Sensing Properties of ZnO Nanowires. *Crystals*, 13, p.1380.

[35] Zaier, A., Meftah, A., Jaber, A.Y., Abdelaziz, A.A. and Aida, M.S., 2015. Annealing effects on the structural, electrical and optical properties of ZnO thin films prepared by thermal evaporation technique. *Journal of King Saud University - Science*, 27, pp.356–360.

[36] Tian, T., Xing, J., Cheng, L., Zheng, L., Ruan, W., Ruan, X. and Li, G., 2015. Synthesis of large size ZnO microrods by a simple way of thermal evaporation. *Ceramics International*, 41, S774–S778.

[37] Jannane, T., Manoua, M., El Hallani, G., Liba, A., Fazouan, N., Almaggoussi, A., El Hichou, A. and Mabrouki, M., 2020. Impact of Sol aging time on structural, morphological, optical and electrical properties of ZnO coatings. *2020 IEEE 6th International Conference on Optimization and Applications (ICOA)* (Beni Mellal, Morocco: IEEE), pp. 1–5.

[38] Bhujel, K., Ningthoujam, S.S., Singh, L.R. and Rai, S., 2021. Effect of solution aging on properties of spin coated zinc oxide thin films. *Materials Today: Proceedings*, 46, pp.6419–6422.

[39] Uma, K., Ananthakumar, S., Mangalaraja, R.V., Soga, T. and Jimbo, T., 2013. Growth and Improvement of ZnO Nanostructure Using Aged Solution by Flow Coating Process. *Advances in Materials Physics and Chemistry*, 03, pp.194–200.

[40] Norhidayah, C.A., Kamaruddin, S.A., Nayan, N., Tawil, S.N.M. and Sahdan, M.Z., 2014. Effects of Ageing Time of ZnO Sol on Properties of ZnO Films by Sol Gel Spin Coating. *Advanced Materials Research*, 925, pp.329–333.

[41] Aghkonbad, E.M., Aghgonbad, M.M. and Sedghi, H., 2019. A Study on Effect of Sol Aging Time on Optical Properties of ZnO Thin Films: Spectroscopic Ellipsometry Method. *Materials and Nanoscale Science*, 11, pp.100–108.

[42] Wojtasik, K., Zięba, M., Tyszkiewicz, C., Pakieła, W., Żak, G., Jeremiasz, O., Gondek, E., Drabczyk, K. and Karasiński, P., 2023. Zinc Oxide Films Fabricated via Sol-Gel Method and Dip-Coating Technique–Effect of Sol Aging on Optical Properties, Morphology and Photocatalytic Activity. *Materials*, 16, p.1898.

[43] Arifin, N.M., Mhd Noor, E.E., Mohamad, F. and Mohamad, N., 2024. The Impact of Spinning Speed on n-TiO2/ZnO Bilayer Thin Film Fabricated through Sol–Gel Spin-Coating Method. *Coatings*, 14, p.73.

[44] Alamdari, S., Jafar Tafreshi, M., Sasani Ghamsari, M. and Majles Ara, M.H., 2021. Preparation and Characterization of ZnO and CWO Nanopowders for Radiation Sensing. *Progress in Physics of Applied Materials*, 1, pp.14–18.

[45] Marasini, S., Pandey, S., Ram Ghimire, R. and Subedi, P., 2025. Effect of Aluminum Doping on the Optical Electrical and Gas Sensing Properties of ZnO Thin Films. *Progress in Physics of Applied Materials*, 5, pp.1–9.

[46] Astinchap, B., Moradian, R. and Nasseri Tekyeh, M., 2016. Investigating the optical properties of synthesized ZnO nanostructures by sol-gel: The role of zinc precursors and annealing time. *Optik*, 127, pp.9871–9877.

[47] Vanaja, A., Jeevanandam, J. and Suresh, M., 2019. Effect of Precursors on Structural and Optical Properties of Sol-Gel Synthesized ZnO

Nanopowders. *Asian Journal of Chemistry*, 31, pp.1825–1829.
[48] Saidani, T., Zaabat, M., Aida, M.S., Barille, R., Rasheed, M. and Almohamed, Y., 2017. Influence of precursor source on sol–gel deposited ZnO thin films properties. *Journal of Materials Science: Materials in Electronics*, 28, pp.9252–9257.
[49] Adl, A.H., Kar, P., Farsinezhad, S., Sharma, H. and Shankar, K., 2015. Effect of sol stabilizer on the structure and electronic properties of solution-processed ZnO thin films. *RSC Advances*, 5, pp.87007–87018.
[50] Nowak, E., Chłopocka, E., Szybowicz, M., Stachowiak, A., Koczorowski, W., Piechowiak, D. and Miklaszewski, A., 2022. The Influence of Aminoalcohols on ZnO Films' Structure. *Gels*, 8, p.512.
[51] Gómez-Núñez, A., Alonso-Gil, S., López, C., Roura, P. and Vilà, A., 2017. Role of Ethanolamine on the Stability of a Sol–Gel ZnO Ink. *Journal of Physical Chemistry C*, 121, pp.23839-23846.
[52] Gboglo, A.D., Baneto, M., Ako, O., Ali-Tagba, A-R., Grandidier, B. and N'konou, K., 2026. Combined Influence of Precursor Source and Solvent Type on Microstructural and Optical Properties of Spin-Coated ZnO Thin Films. *Surfaces*, 9, p.50.
[53] Xu, L., Zheng, G., Miao, J. and Xian, F., 2012. Dependence of structural and optical properties of sol–gel derived ZnO thin films on sol concentration. *Applied Surface Science*, 258, pp.7760-7765.
[54] Speaks, D.T., 2020. Effect of concentration, aging, and annealing on sol gel ZnO and Al-doped ZnO thin films. *International Journal of Mechanical and Materials Engineering*, 15, p.2.
[55] Sanjeev, S. and Kekuda, D., 2015. Effect of Annealing Temperature on the Structural and Optical Properties of Zinc Oxide (ZnO) Thin Films Prepared by Spin Coating Process. *IOP Conference Series: Materials Science and Engineering*, 73, p.012149.
[56] Kim, Y. and Leem, J-Y., 2015. Effect of post-annealing temperature on structural and optical properties of ZnO thin films grown on mica substrates using sol-gel spin-coating. *Journal of the Korean Physical Society*, 67, pp.870–874.
[57] Arif Mohd., Sanger, A., Vilarinho, P.M. and Singh, A., 2018. Effect of Annealing Temperature on Structural and Optical Properties of Sol–Gel-Derived ZnO Thin Films. *Journal of Electronic Materials*, 47, pp.3678–3684.
[58] Singh, A., Kumar, D., Khanna, P.K., Kumar, M. and Prasad, B., 2013. Post annealing effect on structural and optical properties of ZnO thin films derived by sol–gel route. *Journal of Materials Science: Materials in Electronics*, 24, pp.4607–4613.
[59] Elamal Bouzit, S., Bourial, A., Elhichou, A. and Almaggoussi, A., 2013. Temperature annealing effect on structural and optical properties of ZnO thin films prepared by sol-gel method ed A. El Bouari, R. El Ouatib, H. Hannache, S. Krimi, M. Lamire, I. Mansouri, R. Moussa and A. Aboulayt *MATEC Web of Conferences*, 5, p.04007.
[60] Toe, M.Z., Matsuda, A., Yaacob, K.A. and Pung, S.Y., 2024. Influence of Annealing Duration on the Structural, Optical and Electrical Properties of ZnO Layers Deposited Using the Dip-Coating Method. *Engineering International*, 9, pp.1–13.
[61] Kumar, V., Som, S., Yousif, A., Singh, N., Ntwaeaborwa, O.M., Kapoor, A. and Swart, H.C., 2014. Effect of annealing on the structural, morphological and photoluminescence properties of ZnO thin films prepared by spin coating. *Journal of Colloid and Interface Science*, 428, pp.8–15.
[62] Mathew Jijoy, P., Varghese, G. and Mathew, J., 2012. Effect of post-thermal annealing on the structural and optical properties of ZnO thin films prepared from a polymer precursor. *Chinese Physics B*, 21, p.078104.
[63] Motlan, Siregar, N. and Panggabean, J., 2020. The effect of post annealing time on structural and optical properties of ZnO thin films by sol-gel spin coating method. *Journal of Physics: Conference Series*, 1428, p.012065.
[64] Guo, D., Sato, K., Hibino, S., Takeuchi, T., Bessho, H. and Kato, K., 2014. Low-temperature preparation of (002)-oriented ZnO thin films by sol–gel method. *Thin Solid Films*, 550, pp.250-258.
[65] McMurdie, H.F., Morris, M.C., Evans, E.H., Paretzkin, B., Wong-Ng, W., Ettlinger, L. and Hubbard, C.R., 1986. Standard X-Ray Diffraction Powder Patterns from the JCPDS Research Associateship. *Powder Diffraction*, 1, pp.64–77.
[66] Fujimura, N., Nishihara, T., Goto, S. and Xu, J., 1993. Control of preferred orientation for ZnO x films: control of self-texture. *Journal of Crystal Growth*, 130, pp.269–279.
[67] Habibi, M.H. and Khaledi Sardashti, M., 2008. Structure and morphology of nanostructured zinc oxide thin films Prepared by dip-vs. spin-coating methods. *Journal of the Iranian Chemical Society*, 5, pp.603–609.
[68] Ivanova, T., Harizanova, A., Koutzarova, T., Vertruyen, B. and Closset, R., 2022. Deposition of Sol–Gel ZnO:Mg Films and Investigation of Their Structural and Optical Properties. *Materials*, 15, p.8883.
[69] Morinaga, Y., Sakuragi, K., Fujimura, N. and Ito, T., 1997. Effect of Ce doping on the growth of ZnO thin films. *Journal of Crystal Growth*, 174, pp.691–695.
[70] Gboglo, A.D., Baneto, M., Ako, O., Gadedjisso-Tossou, K.S., Grandidier, B., Haris, M., Senthilkumar, M. and N'Konou, K., 2026. Structural, morphological and optical properties of ZnO thin films grown by time-dependent chemical bath deposition. *International Journal of Renewable Energy Development*, 15, pp.66–75.
[71] Kashif, M., Hashim, U., Ali, M.E., Ali, S.M.U., Rusop, M., Ibupoto, Z.H. and Willander, M., 2012. Effect of Different Seed Solutions on the Morphology and Electrooptical Properties of ZnO Nanorods ed G.R. Lin *Journal of Nanomaterials*, 2012, p.6.
[72] Zainab Saad Lafta. and Hayder, J. Al-Asedy., 2025. Studying the effect of annealing time on structural, morphological and optical properties for AZO nanostructures. *JK-Physics*, 17, pp.21–36.

[73] Thongpool, V., Phunpueok, A., Jaiyen, S. and Limsuwan, P., 2026. Williamson-Hall analysis of lattice strain in green-synthesized ZnO nanoparticles using Mitragyna speciosa extract: microstructural insights and antibacterial application. *Results in Physics*, 86, p.108689.

[74] Saidi, M., Ghazi, M. and Izadifard, M., 2023. A Study on Structural Optical and Magnetic Properties of ZnO/ZnFe2O4 Composite. *Progress in Physics of Applied Materials*, 3, pp.49–55.

[75] Khorsand Zak, A. and Hashim, A.M., 2025. Advanced XRD peak broadening analysis of gallium-doped ZnO nanoparticles for crystallite size evaluation. *Scientific Reports*, 16, p.1717.

[76] Mustapha, S., Ndamitso, M.M., Abdulkareem, A.S., Tijani, J.O., Shuaib, D.T., Mohammed, A.K. and Sumaila, A., 2019. Comparative study of crystallite size using Williamson-Hall and Debye-Scherrer plots for ZnO nanoparticles. *Advances in Natural Sciences: Nanoscience and Nanotechnology*, 10, p.045013.

[77] Abdulrahman, A.F., Ahmed, S.M., Hamad, S.M., Almessiere, M.A., Ahmed, N.M. and Sajadi, S.M., 2021. Effect of different pH values on growth solutions for the ZnO nanostructures. *Chinese Journal of Physics*, 71, pp.175–189.

[78] Gboglo, A.D., Baneto, M., Gadedjisso-Tossou, K.S., Ako, O., Ahyi, A.C., Haris, M., Senthilkumar, M., N'konou, K., Grandidier, B., Beltako, K., Amou, K.A. and Dzagli, M.M., 2025. Co-Effect of pH Control Agent and pH Value on the Physical Properties of ZnO Thin Films Obtained by Chemical Bath Deposition for Potential Application in Dye-Sensitized Solar. *Cells Surfaces*, 8, p.46.

[79] Ako, O., Baneto, M., Gboglo, A.D., Senthilkumar, M. and Haris, M., 2025. Temperature-controlled growth of ZnO Thin films by spray pyrolysis: Influence on physical properties for photovoltaic applications. *2576-8484*, 9, pp.1052–1066.

[80] Khiari, M., Gilliot, M., Lejeune, M., Lazar, F. and Hadjadj, A., 2022. Preparation of Very Thin Zinc Oxide Films by Liquid Deposition Process: Review of Key Processing Parameters. *Coatings*, 12, p.65.

[81] Malik, G., Mourya, S., Jaiswal, J. and Chandra, R., 2019. Effect of annealing parameters on optoelectronic properties of highly ordered ZnO thin films. *Materials Science in Semiconductor Processing*, 100, pp.200–213.

[82] Chaitra, U., Kekuda, D. and Mohan Rao, K., 2017. Effect of annealing temperature on the evolution of structural, microstructural, and optical properties of spin coated ZnO thin films. *Ceramics International*, 43, pp.7115–7122.

[83] Faramawy, A., Elsayed, H., Scian, C. and Mattei, G., 2022. Structural, Optical, Magnetic and Electrical Properties of Sputtered ZnO and ZnO:Fe Thin Films: The Role of Deposition Power. *Ceramics*, 5, pp.1128–1153.

[84] Mazur, M., Obstarczyk, A., Posadowski, W., Domaradzki, J., Kiełczawa, S., Wiatrowski, A., Wojcieszak, D., Kalisz, M., Grobelny, M. and Szmidt, J., 2022. Investigation of the Microstructure, Optical, Electrical and Nanomechanical Properties of ZnOx Thin Films Deposited by Magnetron Sputtering. *Materials*, 15, p.6551.

[85] Kaim, P., Lukaszkowicz, K., Szindler, M., Szindler, M.M., Basiaga, M. and Hajduk, B., 2021. The Influence of Magnetron Sputtering Process Temperature on ZnO Thin-Film Properties. *Coatings*, 11, p.1507.

[86] Wuensch, J. and Tuller, H.L., 1994. LATTICE DIFFUSION, GRAIN BOUNDARY DIFFU AND DEFECT STRUCTURE OF ZnO. *Journal of Physics and Chemistry of Solids*, 55, pp.975–984.

[87] Ghica, D., Stefan, M., Ghica, C. and Stan, G.E., 2014. Evaluation of the Segregation of Paramagnetic Impurities at Grain Boundaries in Nanostructured ZnO Films. *ACS Applied Materials and Interfaces*, 6, pp.14231−14238.

[88] Galdámez-Martinez, A., Santana, G., Güell, F., Martínez-Alanis, P.R. and Dutt, A., 2020. Photoluminescence of ZnO Nanowires: A Review. *Nanomaterials*, 10, p.857.

[89] Sokol, A.A., French, S.A., Bromley, S.T., Catlow, C.R.A., Van Dam, H.J.J. and Sherwood, P., 2007. Point defects in ZnO. *Faraday Discussions*, 134, 267–282.

[90] Willander, M., Nur, O., Sadaf, J.R., Qadir, M.I., Zaman, S., Zainelabdin, A., Bano, N. and Hussain, I., 2010. Luminescence from Zinc Oxide Nanostructures and Polymers and their Hybrid Devices. *Materials*, 3, pp.2643–2667.

[91] Vanheusden, K., Seager, C.H., Warren, W.L., Tallant, D.R. and Voigt, J.A., 1996. Correlation between photoluminescence and oxygen vacancies in ZnO phosphors. *Applied Physics Letters*, 68, pp.403–405.

[92] Bhaskar, R., Lakshmanan, A.R., Sundarrajan, M., Ravishankar, T., Jose, M.T. and Lakshminarayan, N., 2009. Mechanism of green luminescence in ZnO. *Indian Journal of Pure & Applied Physics*, 47, pp.772-774.

[93] Quemener, V., Vines, L., Monakhov, E.V. and Svensson, B.G., 2012. Evolution of deep electronic states in ZnO during heat treatment in oxygen- and zinc-rich ambients. *Applied Physics Letters*, 100, p.112108.

[94] Alvi, N.H., Ul Hasan, K., Nur, O. and Willander, M., 2011. The origin of the red emission in n-ZnO nanotubes/p-GaN white light emitting diodes. *Nanoscale Research Letters*, 6, p.130.

[95] Sivakumar, K., Senthil Kumar, V., Thambidurai, M. and Senthil, T.S., 2013. Influence of Annealing Temperature on Nanocrystalline ZnO Thin Films Prepared by Sol-Gel Dip Coating Method. *Advanced Materials Research*, 678, pp.97–102.

[96] Zhang, C., Tu Q., Francis, L.F. and Kortshagen, U.R., 2022. Band Gap Tuning of Films of Undoped ZnO Nanocrystals by Removal of Surface Groups. *Nanomaterials*, 12, p.565.

[97] Mayerhöfer, T.G., Pahlow, S. and Popp, J., 2020. The Bouguer-Beer-Lambert Law: Shining Light on the Obscure. *ChemPhysChem*, 21, pp.2029–2046.

[98] Jubu, P.R., Adedokun O., Mbakaan C., Nathan-Abutu, A., Danladi, E., Tsaviv, J.N., Kyesmen, P.I., Akeredolu B.J., Adepoju, A.T., Aungwa, F., Yusof, Y., Obaseki, O.S., Elzawiei, Y.S. and Pakhuruddin, M.Z., 2025. Accuracy in estimating the absorption coefficient of powdered

nanomaterials: resolving misconceptions in tauc plot application for energy bandgap determination. *Journal of Materials Science: Materials in Electronics*, 36, p.961.

[99] Li, P., Wang, X., Zhang, X., Zhang, L., Yang, X. and Zhao, B., 2019. Investigation of the Charge-Transfer Between Ga-Doped ZnO Nanoparticles and Molecules Using Surface-Enhanced Raman Scattering: Doping Induced Band-Gap Shrinkage. *Frontiers in Chemistry*, 7, p.144.